Measurements of second-harmonic Fourier coefficients from azimuthal anisotropies in math xmlns="http://www.w3.org/1998/Math/MathML">mrow>mi>p/mi>mo>+/mo>mi>p/mi>mo>,/mo>/mrow>/math> math xmlns="http://www.w3.org/1998/Math/MathML">mrow>mi>p/mi>mo>+/mo>mi>Au/mi>mo>,/mo>/mrow>/math> math xmlns="http://www.w3.org/1998/Math/MathML">mrow>mi>d/mi>mo>+/mo>mi>Au/mi>mo>,/mo>/mrow>/math> and math xmlns="http://www.w3.org/1998/Math/MathML">mrow>mmultiscripts>mi>He/mi>mprescripts>/mprescripts>none>/none>mn>3/mn>/mmultiscripts>mo>+/mo>mi>Au/mi>/mrow>/math> collisions at math xmlns="http://www.w3.org/1998/Math/MathML">mrow>msqrt>msub>mi>s/mi>mrow>mi>N/mi>mi>N/mi>/mrow>/msub>/msqrt>mo>=/mo>mn>200/mn>mo> /mo>mi>GeV/mi>/mrow>/math>

N. J. Abdulameer et al. (PHENIX Collaboration)

Phys. Rev. C **107**, 024907 — Published 9 February 2023

DOI: 10.1103/PhysRevC.107.024907

Measurements of second-harmonic Fourier coefficients from azimuthal anisotropies in p+p, p+Au, d+Au, and ^{3}He+Au collisions at $\sqrt{s_{_{NN}}} = 200$ GeV

N.J. Abdulameer,[15] U. Acharya,[20] A. Adare,[12] C. Aidala,[42] N.N. Ajitanand,[61,*] Y. Akiba,[56,57,†] M. Alfred,[22] V. Andrieux,[42] K. Aoki,[31,56] N. Apadula,[27,62] H. Asano,[34,56] C. Ayuso,[42] B. Azmoun,[7] V. Babintsev,[23] M. Bai,[6] N.S. Bandara,[40] B. Bannier,[62] K.N. Barish,[8] S. Bathe,[5,57] A. Bazilevsky,[7] M. Beaumier,[8] S. Beckman,[12] R. Belmont,[12,42,49] A. Berdnikov,[59] Y. Berdnikov,[59] L. Bichon,[67] B. Blankenship,[67] D.S. Blau,[33,46] M. Boer,[36] J.S. Bok,[48] V. Borisov,[59] K. Boyle,[57] M.L. Brooks,[36] J. Bryslawskyj,[5,8] V. Bumazhnov,[23] C. Butler,[20] S. Campbell,[13,27] V. Canoa Roman,[62] R. Cervantes,[62] C.-H. Chen,[57] M. Chiu,[7] C.Y. Chi,[13] I.J. Choi,[24] J.B. Choi,[29,*] T. Chujo,[66] Z. Citron,[68] M. Connors,[20,57] R. Corliss,[62] Y. Corrales Morales,[36] N. Cronin,[44,62] M. Csanád,[16] T. Csörgő,[41,69] L. D. Liu,[53] T.W. Danley,[50] A. Datta,[47] M.S. Daugherity,[1] G. David,[7,62] C.T. Dean,[36] K. DeBlasio,[47] K. Dehmelt,[62] A. Denisov,[23] A. Deshpande,[57,62] E.J. Desmond,[7] A. Dion,[62] P.B. Diss,[39] D. Dixit,[62] V. Doomra,[62] J.H. Do,[70] A. Drees,[62] K.A. Drees,[6] M. Dumancic,[68] J.M. Durham,[36] A. Durum,[23] T. Elder,[20] H. En'yo,[56] A. Enokizono,[56,58] R. Esha,[62] B. Fadem,[44] W. Fan,[62] N. Feege,[62] D.E. Fields,[47] M. Finger, Jr.,[9] M. Finger,[9] D. Firak,[15,62] D. Fitzgerald,[42] S.L. Fokin,[33] J.E. Frantz,[50] A. Franz,[7] A.D. Frawley,[19] Y. Fukuda,[66] P. Gallus,[14] C. Gal,[62] P. Garg,[3,62] H. Ge,[62] M. Giles,[62] F. Giordano,[24] A. Glenn,[35] Y. Goto,[56,57] N. Grau,[2] S.V. Greene,[67] M. Grosse Perdekamp,[24] T. Gunji,[11] H. Guragain,[20] T. Hachiya,[45,56,57] J.S. Haggerty,[7] K.I. Hahn,[17] H. Hamagaki,[11] H.F. Hamilton,[1] J. Hanks,[62] S.Y. Han,[17,32] M. Harvey,[64] S. Hasegawa,[28] T.O.S. Haseler,[20] K. Hashimoto,[56,58] T.K. Hemmick,[62] X. He,[20] J.C. Hill,[27] K. Hill,[12] A. Hodges,[20,24] R.S. Hollis,[8] K. Homma,[21] B. Hong,[32] T. Hoshino,[21] N. Hotvedt,[27] J. Huang,[7] K. Imai,[28] J. Imrek,[15] M. Inaba,[66] A. Iordanova,[8] D. Isenhower,[1] Y. Ito,[45] D. Ivanishchev,[54] B.V. Jacak,[62] M. Jezghani,[20] X. Jiang,[36] Z. Ji,[62] B.M. Johnson,[7,20] V. Jorjadze,[62] D. Jouan,[52] D.S. Jumper,[24] S. Kanda,[11] J.H. Kang,[70] D. Kapukchyan,[8] S. Karthas,[62] D. Kawall,[40] A.V. Kazantsev,[33] J.A. Key,[47] V. Khachatryan,[62] A. Khanzadeev,[54] A. Khatiwada,[36] B. Kimelman,[44] C. Kim,[8,32] D.J. Kim,[30] E.-J. Kim,[29] G.W. Kim,[17] M. Kim,[60] M.H. Kim,[32] T. Kim,[17] D. Kincses,[16] A. Kingan,[62] E. Kistenev,[7] R. Kitamura,[11] J. Klatsky,[19] D. Kleinjan,[8] P. Kline,[62] T. Koblesky,[12] B. Komkov,[54] D. Kotov,[54,59] L. Kovacs,[16] S. Kudo,[66] B. Kurgyis,[16,62] K. Kurita,[58] M. Kurosawa,[56,57] Y. Kwon,[70] J.G. Lajoie,[27] E.O. Lallow,[44] D. Larionova,[59] A. Lebedev,[27] S. Lee,[70] S.H. Lee,[27,42,62] M.J. Leitch,[36] Y.H. Leung,[62] N.A. Lewis,[42] S.H. Lim,[36,55,70] M.X. Liu,[36] X. Li,[10] X. Li,[36] V.-R. Loggins,[24] D.A. Loomis,[42] K. Lovasz,[15] D. Lynch,[7] S. Lökös,[16] T. Majoros,[15] Y.I. Makdisi,[6] M. Makek,[71] M. Malaev,[54] A. Manion,[62] V.I. Manko,[33] E. Mannel,[7] H. Masuda,[58] M. McCumber,[36] P.L. McGaughey,[36] D. McGlinchey,[12,36] C. McKinney,[24] A. Meles,[48] M. Mendoza,[8] A.C. Mignerey,[39] D.E. Mihalik,[62] A. Milov,[68] D.K. Mishra,[4] J.T. Mitchell,[7] M. Mitrankova,[59] Iu. Mitrankov,[59] G. Mitsuka,[31,57] S. Miyasaka,[56,65] S. Mizuno,[56,66] A.K. Mohanty,[4] M.M. Mondal,[62] P. Montuenga,[24] T. Moon,[32,70] D.P. Morrison,[7] S.I. Morrow,[67] T.V. Moukhanova,[33] B. Mulilo,[32,56,72] T. Murakami,[34,56] J. Murata,[56,58] A. Mwai,[61] K. Nagai,[65] K. Nagashima,[21] T. Nagashima,[58] J.L. Nagle,[12] M.I. Nagy,[16] I. Nakagawa,[56,57] H. Nakagomi,[56,66] K. Nakano,[56,65] C. Nattrass,[63] S. Nelson,[18] P.K. Netrakanti,[4] T. Niida,[66] S. Nishimura,[11] R. Nouicer,[7,57] N. Novitzky,[30,62,66] R. Novotny,[14] T. Novák,[41,69] G. Nukazuka,[56,57] A.S. Nyanin,[33] E. O'Brien,[7] C.A. Ogilvie,[27] J.D. Orjuela Koop,[12] M. Orosz,[15] J.D. Osborn,[42,51] A. Oskarsson,[37] G.J. Ottino,[47] K. Ozawa,[31,66] R. Pak,[7] V. Pantuev,[25] V. Papavassiliou,[48] J.S. Park,[60] S. Park,[43,56,60,62] M. Patel,[27] S.F. Pate,[48] J.-C. Peng,[24] W. Peng,[67] D.V. Perepelitsa,[7,12] G.D.N. Perera,[48] D.Yu. Peressounko,[33] C.E. PerezLara,[62] J. Perry,[27] R. Petti,[7,62] M. Phipps,[7,24] C. Pinkenburg,[7] R. Pinson,[1] R.P. Pisani,[7] M. Potekhin,[7] A. Pun,[50] M.L. Purschke,[7] P.V. Radzevich,[59] J. Rak,[30] N. Ramasubramanian,[62] B.J. Ramson,[42] I. Ravinovich,[68] K.F. Read,[51,63] D. Reynolds,[61] V. Riabov,[46,54] Y. Riabov,[54,59] D. Richford,[5] T. Rinn,[24,27] S.D. Rolnick,[8] M. Rosati,[27] Z. Rowan,[5] J.G. Rubin,[42] J. Runchey,[27] A.S. Safonov,[59] B. Sahlmueller,[62] N. Saito,[31] T. Sakaguchi,[7] H. Sako,[28] V. Samsonov,[46,54] M. Sarsour,[20] K. Sato,[66] S. Sato,[28] B. Schaefer,[67] B.K. Schmoll,[63] K. Sedgwick,[8] R. Seidl,[56,57] A. Sen,[27,63] R. Seto,[8] P. Sett,[4] A. Sexton,[39] D. Sharma,[62] I. Shein,[23] M. Shibata,[45] T.-A. Shibata,[56,65] K. Shigaki,[21] M. Shimomura,[27,45] T. Shioya,[66] Z. Shi,[36] P. Shukla,[4] A. Sickles,[7,24] C.L. Silva,[36] D. Silvermyr,[37,51] B.K. Singh,[3] C.P. Singh,[3] V. Singh,[3] M. Slunečka,[9] K.L. Smith,[19] M. Snowball,[36] R.A. Soltz,[35] W.E. Sondheim,[36] S.P. Sorensen,[63] I.V. Sourikova,[7] P.W. Stankus,[51] M. Stepanov,[40,*] S.P. Stoll,[7] T. Sugitate,[21] A. Sukhanov,[7] T. Sumita,[56] J. Sun,[62] Z. Sun,[15] S. Syed,[20] J. Sziklai,[69] R. Takahama,[45] A. Takeda,[45] A. Taketani,[56,57] K. Tanida,[28,57,60] M.J. Tannenbaum,[7] S. Tarafdar,[67,68] A. Taranenko,[46,61] G. Tarnai,[15] R. Tieulent,[20,38] A. Timilsina,[27] T. Todoroki,[56,57,66] M. Tomášek,[14] C.L. Towell,[1] R. Towell,[1] R.S. Towell,[1] I. Tserruya,[68] Y. Ueda,[21] B. Ujvari,[15] H.W. van Hecke,[36] S. Vazquez-Carson,[12] J. Velkovska,[67] M. Virius,[14] V. Vrba,[14,26] N. Vukman,[71] X.R. Wang,[48,57] Z. Wang,[5] Y. Watanabe,[56,57] Y.S. Watanabe,[11,31] F. Wei,[48] A.S. White,[42] C.P. Wong,[20,20,36] C.L. Woody,[7] M. Wysocki,[51] B. Xia,[50] L. Xue,[20] C. Xu,[48] Q. Xu,[67] S. Yalcin,[62] Y.L. Yamaguchi,[11,57,62] H. Yamamoto,[66] A. Yanovich,[23] P. Yin,[12] I. Yoon,[60] J.H. Yoo,[32] I.E. Yushmanov,[33] H. Yu,[48,53] W.A. Zajc,[13] A. Zelenski,[6] S. Zhou,[10] and L. Zou[8]

(PHENIX Collaboration)

[1]*Abilene Christian University, Abilene, Texas 79699, USA*
[2]*Department of Physics, Augustana University, Sioux Falls, South Dakota 57197, USA*
[3]*Department of Physics, Banaras Hindu University, Varanasi 221005, India*
[4]*Bhabha Atomic Research Centre, Bombay 400 085, India*
[5]*Baruch College, City University of New York, New York, New York, 10010 USA*
[6]*Collider-Accelerator Department, Brookhaven National Laboratory, Upton, New York 11973-5000, USA*
[7]*Physics Department, Brookhaven National Laboratory, Upton, New York 11973-5000, USA*
[8]*University of California-Riverside, Riverside, California 92521, USA*
[9]*Charles University, Faculty of Mathematics and Physics, 180 00 Troja, Prague, Czech Republic*
[10]*Science and Technology on Nuclear Data Laboratory, China Institute of Atomic Energy, Beijing 102413, People's Republic of China*
[11]*Center for Nuclear Study, Graduate School of Science, University of Tokyo, 7-3-1 Hongo, Bunkyo, Tokyo 113-0033, Japan*
[12]*University of Colorado, Boulder, Colorado 80309, USA*
[13]*Columbia University, New York, New York 10027 and Nevis Laboratories, Irvington, New York 10533, USA*
[14]*Czech Technical University, Zikova 4, 166 36 Prague 6, Czech Republic*
[15]*Debrecen University, H-4010 Debrecen, Egyetem tér 1, Hungary*
[16]*ELTE, Eötvös Loránd University, H-1117 Budapest, Pázmány P. s. 1/A, Hungary*
[17]*Ewha Womans University, Seoul 120-750, Korea*
[18]*Florida A&M University, Tallahassee, FL 32307, USA*
[19]*Florida State University, Tallahassee, Florida 32306, USA*
[20]*Georgia State University, Atlanta, Georgia 30303, USA*
[21]*Hiroshima University, Kagamiyama, Higashi-Hiroshima 739-8526, Japan*
[22]*Department of Physics and Astronomy, Howard University, Washington, DC 20059, USA*
[23]*IHEP Protvino, State Research Center of Russian Federation, Institute for High Energy Physics, Protvino, 142281, Russia*
[24]*University of Illinois at Urbana-Champaign, Urbana, Illinois 61801, USA*
[25]*Institute for Nuclear Research of the Russian Academy of Sciences, prospekt 60-letiya Oktyabrya 7a, Moscow 117312, Russia*
[26]*Institute of Physics, Academy of Sciences of the Czech Republic, Na Slovance 2, 182 21 Prague 8, Czech Republic*
[27]*Iowa State University, Ames, Iowa 50011, USA*
[28]*Advanced Science Research Center, Japan Atomic Energy Agency, 2-4 Shirakata Shirane, Tokai-mura, Naka-gun, Ibaraki-ken 319-1195, Japan*
[29]*Jeonbuk National University, Jeonju, 54896, Korea*
[30]*Helsinki Institute of Physics and University of Jyväskylä, P.O.Box 35, FI-40014 Jyväskylä, Finland*
[31]*KEK, High Energy Accelerator Research Organization, Tsukuba, Ibaraki 305-0801, Japan*
[32]*Korea University, Seoul 02841, Korea*
[33]*National Research Center "Kurchatov Institute", Moscow, 123098 Russia*
[34]*Kyoto University, Kyoto 606-8502, Japan*
[35]*Lawrence Livermore National Laboratory, Livermore, California 94550, USA*
[36]*Los Alamos National Laboratory, Los Alamos, New Mexico 87545, USA*
[37]*Department of Physics, Lund University, Box 118, SE-221 00 Lund, Sweden*
[38]*IPNL, CNRS/IN2P3, Univ Lyon, Université Lyon 1, F-69622, Villeurbanne, France*
[39]*University of Maryland, College Park, Maryland 20742, USA*
[40]*Department of Physics, University of Massachusetts, Amherst, Massachusetts 01003-9337, USA*
[41]*MATE, Laboratory of Femtoscopy, Károly Róbert Campus, H-3200 Gyöngyös, Mátraiút 36, Hungary*
[42]*Department of Physics, University of Michigan, Ann Arbor, Michigan 48109-1040, USA*
[43]*Mississippi State University, Mississippi State, Mississippi 39762, USA*
[44]*Muhlenberg College, Allentown, Pennsylvania 18104-5586, USA*
[45]*Nara Women's University, Kita-uoya Nishi-machi Nara 630-8506, Japan*
[46]*National Research Nuclear University, MEPhI, Moscow Engineering Physics Institute, Moscow, 115409, Russia*
[47]*University of New Mexico, Albuquerque, New Mexico 87131, USA*
[48]*New Mexico State University, Las Cruces, New Mexico 88003, USA*
[49]*Physics and Astronomy Department, University of North Carolina at Greensboro, Greensboro, North Carolina 27412, USA*
[50]*Department of Physics and Astronomy, Ohio University, Athens, Ohio 45701, USA*
[51]*Oak Ridge National Laboratory, Oak Ridge, Tennessee 37831, USA*
[52]*IPN-Orsay, Univ. Paris-Sud, CNRS/IN2P3, Université Paris-Saclay, BP1, F-91406, Orsay, France*
[53]*Peking University, Beijing 100871, People's Republic of China*
[54]*PNPI, Petersburg Nuclear Physics Institute, Gatchina, Leningrad region, 188300, Russia*
[55]*Pusan National University, Pusan 46241, Korea*
[56]*RIKEN Nishina Center for Accelerator-Based Science, Wako, Saitama 351-0198, Japan*
[57]*RIKEN BNL Research Center, Brookhaven National Laboratory, Upton, New York 11973-5000, USA*

[58] Physics Department, Rikkyo University, 3-34-1 Nishi-Ikebukuro, Toshima, Tokyo 171-8501, Japan
[59] Saint Petersburg State Polytechnic University, St. Petersburg, 195251 Russia
[60] Department of Physics and Astronomy, Seoul National University, Seoul 151-742, Korea
[61] Chemistry Department, Stony Brook University, SUNY, Stony Brook, New York 11794-3400, USA
[62] Department of Physics and Astronomy, Stony Brook University, SUNY, Stony Brook, New York 11794-3800, USA
[63] University of Tennessee, Knoxville, Tennessee 37996, USA
[64] Texas Southern University, Houston, TX 77004, USA
[65] Department of Physics, Tokyo Institute of Technology, Oh-okayama, Meguro, Tokyo 152-8551, Japan
[66] Tomonaga Center for the History of the Universe, University of Tsukuba, Tsukuba, Ibaraki 305, Japan
[67] Vanderbilt University, Nashville, Tennessee 37235, USA
[68] Weizmann Institute, Rehovot 76100, Israel
[69] Institute for Particle and Nuclear Physics, Wigner Research Centre for Physics, Hungarian Academy of Sciences (Wigner RCP, RMKI) H-1525 Budapest 114, POBox 49, Budapest, Hungary
[70] Yonsei University, IPAP, Seoul 120-749, Korea
[71] Department of Physics, Faculty of Science, University of Zagreb, Bijenička c. 32 HR-10002 Zagreb, Croatia
[72] Department of Physics, School of Natural Sciences, University of Zambia, Great East Road Campus, Box 32379, Lusaka, Zambia

(Dated: December 19, 2022)

Recently, the PHENIX Collaboration has published second- and third-harmonic Fourier coefficients v_2 and v_3 for midrapidity ($|\eta| < 0.35$) charged hadrons in 0%–5% central p+Au, d+Au, and ^{3}He+Au collisions at $\sqrt{s_{_{NN}}} = 200$ GeV utilizing three sets of two-particle correlations for two detector combinations with different pseudorapidity acceptance [Phys. Rev. C **105**, 024901 (2022)]. This paper extends these measurements of v_2 to all centralities in p+Au, d+Au, and ^{3}He+Au collisions, as well as p+p collisions, as a function of transverse momentum (p_T) and event multiplicity. The kinematic dependence of v_2 is quantified as the ratio R of v_2 between the two detector combinations as a function of event multiplicity for $0.5<p_T<1$ and $2<p_T<2.5$ GeV/c. A multiphase-transport (AMPT) model can reproduce the observed v_2 in most-central to midcentral d+Au and ^{3}He+Au collisions. However, the AMPT model systematically overestimates the measurements in p+p, p+Au, and peripheral d+Au and ^{3}He+Au collisions, indicating a higher nonflow contribution in AMPT than in the experimental data. The AMPT model fails to describe the observed R for $0.5<p_T<1$ GeV/c, but there is qualitative agreement with the measurements for $2<p_T<2.5$ GeV/c.

I. INTRODUCTION

Observations of azimuthal anisotropy in the emission of produced particles in high-energy heavy-ion collisions at the Relativistic Heavy Ion Collider (RHIC) are considered to be strong evidence of the formation of the quark-gluon plasma (QGP) [1–4]. The measured anisotropy at RHIC and the Large Hadron Collider, quantified via Fourier coefficients v_n of the final-state particle yield relative to the participant plane, is successfully reproduced by viscous hydrodynamic calculations [5, 6]. These theoretical analyses of the experimental v_n data suggest that the collision geometry is translated into the final state momentum space via the hydrodynamic expansion of the QGP.

Heavy-ion experiments have also studied cold-nuclear-matter effects as potential backgrounds for QGP measurements, utilizing small collision systems, consisting of a light nucleus colliding with a heavy nucleus, where QGP formation had not been expected due to the small system size and low multiplicity. However, azimuthal anisotropy similar to that found in large collision systems has also been observed in high-multiplicity p+Pb collisions at $\sqrt{s_{_{NN}}} = 5.02$ TeV at the Large Hadron Collider [7–9] and in high-multiplicity d+Au collisions at $\sqrt{s_{_{NN}}} = 200$ GeV at RHIC [10]. These surprising measurements raised the question of whether the v_n originates from the hydrodynamic expansion of the initial collision geometry in such small collision systems as well.

To address this question, it was proposed to experimentally examine the initial geometry dependence of the medium expansion, empirically known to hold in heavy-ion collisions, using the second- and third-harmonic azimuthal anisotropies v_2 and v_3 [11]. For this purpose, from 2014 to 2016, RHIC delivered p+Au, d+Au, and ^{3}He+Au collisions at $\sqrt{s_{_{NN}}} = 200$ GeV. The series of v_n measurements with these data sets by the PHENIX Collaboration [12–15], culminating in the complete set of results published in Nature Physics [16], show that v_2 and v_3 follow the pattern of the second- and third-harmonic initial eccentricities ε_2 and ε_3 estimated using the Monte Carlo-Glauber model. This observed relationship between initial geometry and final state correlations serves as evidence for QGP formation in

[*] Deceased
[†] PHENIX Spokesperson: akiba@rcf.rhic.bnl.gov

small collision systems. The STAR Collaboration reported that v_2/ε_2, as a function of charged particle multiplicity to the minus-one-third power $\langle N_{ch}\rangle^{-1/3}$, forms a common curve among high-multiplicity small- and large-system collisions [17], which also implies the same underlying physics processes in such collision systems.

Additional hydrodynamic predictions with MC-Glauber initial conditions [18] also successfully reproduced the observed data, which corroborates formation of the QGP in small collision systems. Contrariwise, calculations based solely on initial-state correlations in the color-glass-condensate effective-field-theory formalism [19, 20] are ruled out by the experimental data.

Furthermore, some hydrodynamic calculations incorporate the effect of prehydrodynamization parton dynamics with the weak [21] and strong [22] coupling limits. Both calculations are in quantitative agreement with the experimental data. However, the size of the prehydrodynamization dynamics cannot be determined with the current experimental and theoretical uncertainties. A systematic study of the collision-system and energy dependences in the hydrodynamic calculations [23] indicates the contribution of the prehydrodynamization dynamics becomes more pronounced in smaller collisions and at lower energies, where the QGP medium has a shorter lifetime. Extending experimental measurements to even smaller systems than high-multiplicity p+Au, d+Au, and ^{3}He+Au collisions can provide additional insights into the prehydrodynamization dynamics.

More recently, the PHENIX Collaboration has reported v_2 and v_3 in 0%–5% central p+Au, d+Au, and ^{3}He+Au collisions at $\sqrt{s_{_{NN}}} = 200$ GeV obtained with three sets of two-particle correlations (2PC) for two detector combinations with different pseudorapidity acceptance [24]. One set of those measurements used the same detectors, i.e. two detectors at backward rapidity (the Au-going direction) and one at midrapidity, and found good agreement between the 3×2PC method results and the event plane method results reported in Ref. [16]. Another set of those measurements included a detector located at forward rapidity ($p/d/^3$He-going direction), which results in significantly larger v_2 values and imaginary v_3 in p+Au and d+Au collisions. A careful analysis [25] of these experimental measurements suggests substantial nonflow contributions at forward rapidity because of both low multiplicity and possible longitudinal decorrelation effects. Estimating the multiplicity dependence of these effects would also be of interest to understand flow patterns in small systems.

In this article, our earlier v_2 measurements [24] are extended from most-central to peripheral p+Au, d+Au, and ^{3}He+Au collisions, as well as p+p collisions, as a function of transverse momentum (p_T) and event multiplicity. These measurements provide experimental data with different fractional contributions of prehydrodynamization, nonflow, and decorrelation effects. We also compare these measurements with a multiphase transport (AMPT) model [26] calculations, and the implications for nonflow and event-plane decorrelation effects in the kinematic selection dependence of v_2 are discussed.

II. ANALYSIS METHODOLOGY

This section details the detector subsystems of the PHENIX experiment, the analysis method employed, and the assessment of systematic uncertainties in this analysis.

A. PHENIX Detectors

The east and west central arms (CNT) [27] reconstruct charged particle tracks using the drift chambers and pad-chamber layers. Each arm covers a pseudorapidity range of $|\eta| < 0.35$ with an azimuthal (ϕ) coverage of $\pi/2$. The drift chambers determine the track momentum and the pad chambers reject background tracks by requiring that the track hits be within two standard deviations of their associated projections. In this analysis, CNT tracks below $p_T = 4$ GeV/c are used to avoid background tracks from conversion electrons at high p_T.

The forward-silicon-vertex (FVTX) detectors [28] are installed in both the negative-rapidity south-side region (Au-going direction) and the positive-rapidity north-side region ($p/d/^3$He-going direction), covering $1 < |\eta| < 3$ with full 2π azimuthal acceptance. Both the south-side FVTX (FVTXS) and north-side FVTX (FVTXN) are used in this analysis. Charged particles within the acceptance of $1.2 < |\eta| < 2.2$ and transverse momentum of $p_T > 0.3$ GeV/c are reconstructed using the FVTX. The FVTX does not provide momentum information for tracks because of the orientation of the FVTX strips relative to the magnetic field. The FVTX also provides the distance of closest approach to the primary collision vertex in the transverse direction to the beam axis (DCA$_R$) with a resolution of 1.2 cm at $p_T = 0.5$ GeV/c. Tracks with $|\mathrm{DCA}_R| < 2$ cm are used in this analysis to reject background tracks.

Two beam-beam counters (BBC) [29] are arrayed around the beam pipe at ±144 cm from the nominal beam interaction point in both the south-side and north-side regions, covering the pseudorapidity range of $3.1 < |\eta| < 3.9$ with full 2π azimuthal acceptance. Each BBC comprises 64 Čerenkov radiators equipped with a photomultiplier tube (PMT) and measures the total charge deposited in its acceptance, which is proportional to the number of particles.

The BBC triggers on minimum-bias (MB) p+p, p+Au, d+Au, and ^{3}He+Au collisions by requiring at least one hit on each side. The MB trigger efficiency is 55±5%, 84±3%, 88±4%, and 88±4% for inelastic p+p, p+Au, d+Au, and ^{3}He+Au collisions, respectively. Triggered events are further required to have an online z-vertex within $|z| < 10$ cm in this analysis. The collision centralities in p+Au, d+Au, and ^{3}He+Au collisions are determined using the total charge in the south-side BBC (BBCS), as described in Ref. [30]. The high-multiplicity trigger additionally required more than 35, 40, 49 hit tubes in the BBCS for p+Au, d+Au, and ^{3}He+Au collisions, respectively. In Ref [16], the high-multiplicity trigger is used to improve the statistics of the 0%–5% centrality selection. In the present analysis, for more peripheral collisions only the MB trigger is used.

The instantaneous luminosities delivered by RHIC for p+p, p+Au, d+Au, and ^{3}He+Au collisions at $\sqrt{s_{_{NN}}} = 200$ GeV during 2014, 2015, and 2016 were high enough to record multiple collisions (i.e. pileup). Typically multiple collisions occur at different positions along the beam direction, which is reflected as broader or secondary peaks in the timing distribution of hits in the BBCS. In each event, this shape is quantified as the fraction f of the BBCS hits that have times within a 0.5 ns window from the most probable value of the measured timing distribution, as was done in Ref. [13]. Pileup events are rejected by requiring $f > 0.9$.

B. The 3×2PC method

In this analysis, the two-particle correlation method is employed. Because of the asymmetry in both the multiplicity and v_n as a function of pseudorapidity [31], two-particle azimuthal correlations are constructed with three different sets of pairs. This method was developed in Ref. [24] and is called the 3×2PC method.

The 2PC function $C(\Delta\phi)$ is defined as

$$C(\Delta\phi) = \frac{S(\Delta\phi)}{M(\Delta\phi)} \frac{\int_0^{2\pi} d\Delta\phi M(\Delta\phi)}{\int_0^{2\pi} d\Delta\phi S(\Delta\phi)}, \tag{1}$$

$$S(\Delta\phi) = \frac{dN_{\rm same}(\Delta\phi) \times w}{d\Delta\phi}, \tag{2}$$

$$M(\Delta\phi) = \frac{dN_{\rm mixed}(\Delta\phi) \times w}{d\Delta\phi}, \tag{3}$$

where $\Delta\phi$ is the difference in the azimuthal angles between two particles, $S(\Delta\phi)$ is the foreground distribution constructed from track pairs in the same event $N_{\rm same}$, and $M(\Delta\phi)$ is the mixed event distribution constructed from track pairs from different events $N_{\rm mixed}$ in the same centrality and collision vertex class. The weight w is 1 when correlating with tracks and the charge in the PMT when correlating with BBC PMTs.

We fit the correlation functions with a Fourier series up to the fourth harmonic:

$$F(\Delta\phi) = 1 + \sum_{n=1}^{4} 2c_n \cos n\Delta\phi, \tag{4}$$

where $c_n = \langle \cos n\Delta\phi \rangle$ is the n-th harmonic Fourier component and n is the harmonic number. Under the flow-factorization assumption, the obtained c_n can be related to v_n as

$$c_n^{AB} = \langle v_n^A v_n^B \rangle, \tag{5}$$

$$c_n^{AC} = \langle v_n^A v_n^C \rangle, \tag{6}$$

$$c_n^{BC} = \langle v_n^B v_n^C \rangle, \tag{7}$$

where A, B, and C stand for sub events used to measure correlation functions. Finally, v_n is obtained as

$$v_n^C\{3 \times 2\mathrm{PC}\}({p_T}^C) = \sqrt{\frac{c_n^{AC}({p_T}^C) \times c_n^{BC}({p_T}^C)}{c_n^{AB}}}, \tag{8}$$

letting the sub-event C be CNT for the midrapidity v_n measurements presented in this manuscript. Here we assume that detector effects in the sub events A and B are canceled out between the numerator and denominator inside the square root of Eq. (8).

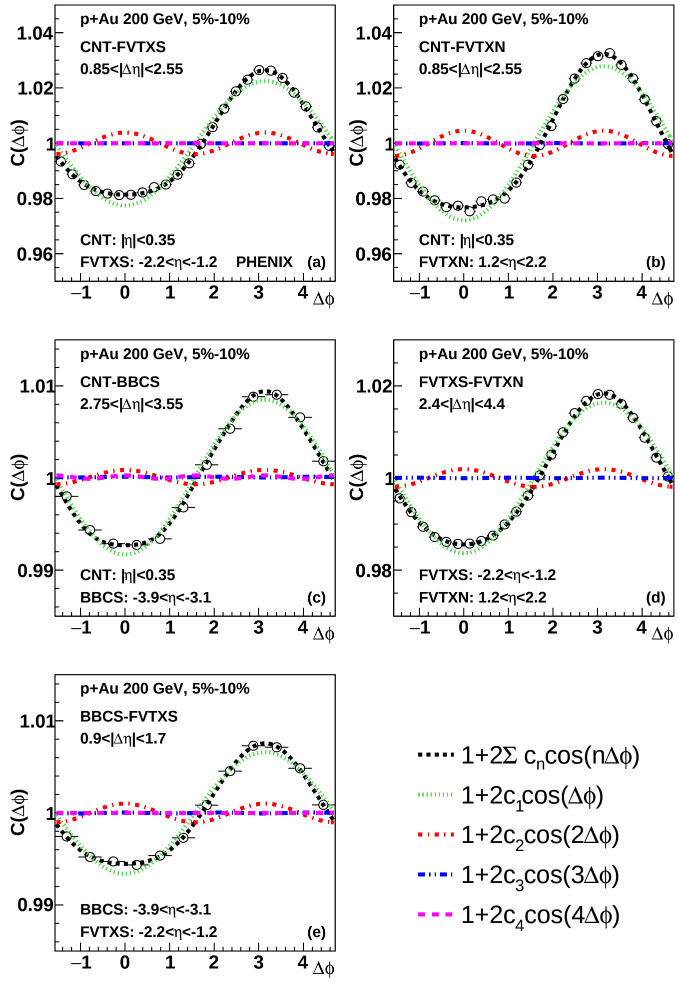

FIG. 1. Correlation functions $C(\Delta\phi)$ in 5%–10% centrality p+Au collisions at $\sqrt{s_{NN}} = 200$ GeV measured using (a) CNT-FVTXS, (b) CNT-FVTXN, (c) CNT-BBCS, (d) FVTXS-FVTXN, and (e) BBCS-FVTXS detector combinations. The short-dashed [black] curve shows the Fourier fit to correlation functions. The dotted [green], dash-dotted [red], dashed-double-dotted [blue], and long-dashed [magenta] curves indicate c_1, c_2, c_3, and c_4 components, respectively.

Figures 1, 2, and 3 show $C(\Delta\phi)$ and the Fourier fits to $C(\Delta\phi)$ in 5%–10% central p+Au, d+Au, and ^{3}He+Au collisions at $\sqrt{s_{NN}} = 200$ GeV, respectively. In each panel of Figs. 1, 2, and 3, correlations are measured between

(a) CNT tracks and FVTXS tracks,
(b) CNT tracks and FVTXN tracks,
(c) CNT tracks and BBCS tubes,
(d) FVTXS and FVTXN tracks, and
(e) BBCS tubes and FVTXS tracks,

where CNT tracks are required to be $0.2 < p_T < 4$ GeV/c. The rapidity coverage of these detectors and rapidity gaps between the detector pairs used for the correlation functions are specified in each panel. See also Ref. [24] for the correlation functions in MB p+p and 0%–5% central p+Au, d+Au, and ^{3}He+Au collisions.

Notably, a nonzero value of the second-harmonic coefficient c_2 is observed also in noncentral collisions for these correlation functions. Thus v_2 can be measured in noncentral collisions with the 3×2PC method using the BBCS-FVTXS-CNT and FVTXS-CNT-FVTXN detector combinations as done for 0%–5% collisions in Ref. [24]. The former combination BBCS-FVTXS-CNT is denoted as "BB" as it uses two detectors located at backward rapidity. Similarly, the latter combination FVTXS-CNT-FVTXN is called "BF" as it uses one detector at backward rapidity and another detector at forward rapidity.

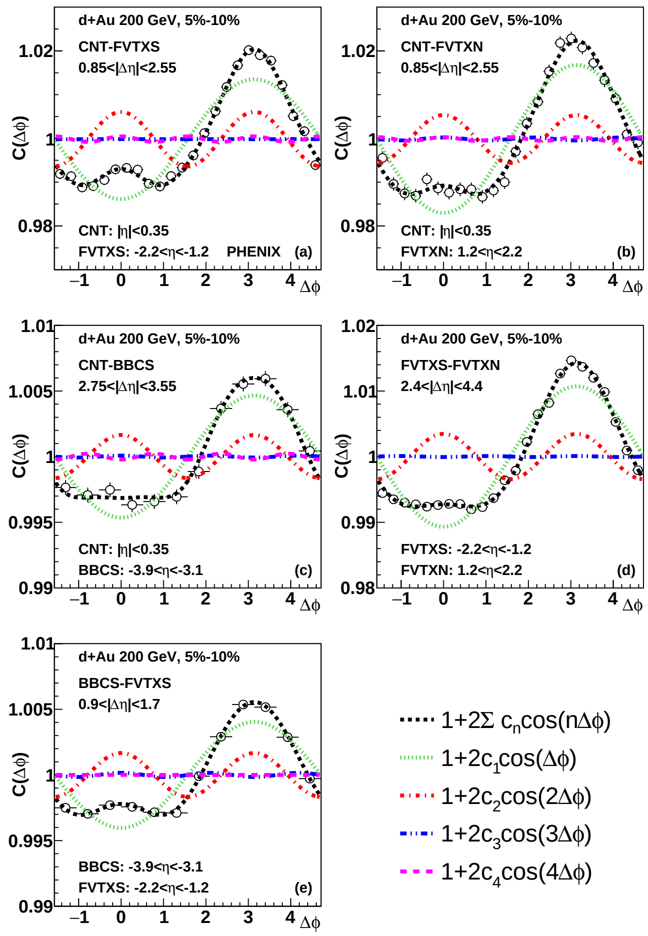

FIG. 2. Correlation functions $C(\Delta\phi)$ in 5%–10% centrality d+Au collisions at $\sqrt{s_{NN}} = 200$ GeV measured using (a) CNT-FVTXS, (b) CNT-FVTXN, (c) CNT-BBCS, (d) FVTXS-FVTXN, and (e) BBCS-FVTXS detector combinations. The short-dashed [black] curve shows the Fourier fit to correlation functions. The dotted [green], dash-dotted [red], dashed-double-dotted [blue], and long-dashed [magenta] curves indicate c_1, c_2, c_3, and c_4 components, respectively.

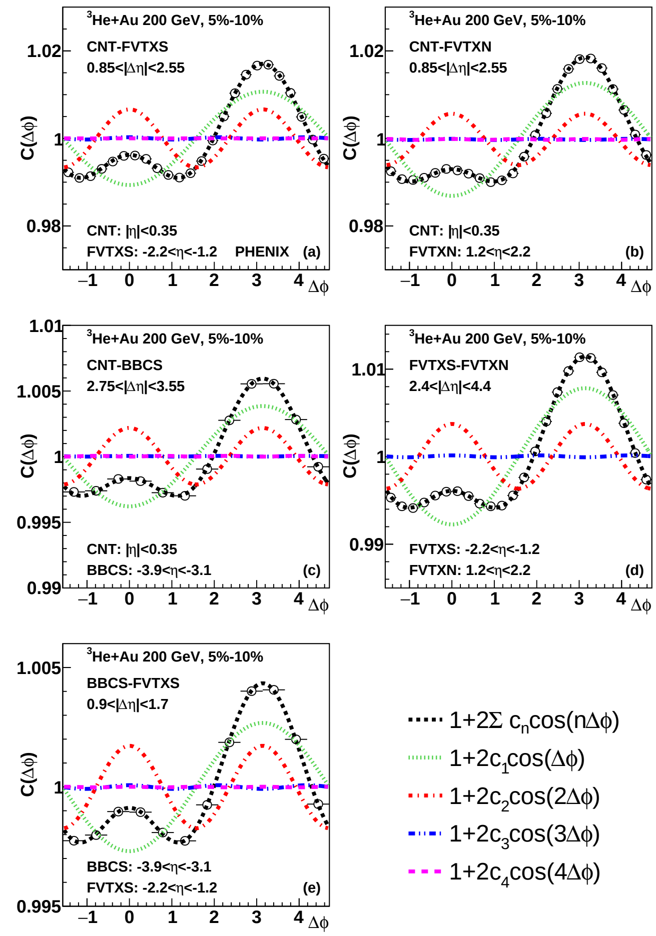

FIG. 3. Correlation functions $C(\Delta\phi)$ in 5%–10% centrality ^{3}He+Au collisions at $\sqrt{s_{NN}} = 200$ GeV measured using (a) CNT-FVTXS, (b) CNT-FVTXN, (c) CNT-BBCS, (d) FVTXS-FVTXN, and (e) BBCS-FVTXS detector combinations. The short-dashed [black] curve shows the Fourier fit to correlation functions. The dotted [green], dash-dotted [red], dashed-double-dotted [blue], and long-dashed [magenta] curves indicate c_1, c_2, c_3, and c_4 components, respectively.

C. Systematic Uncertainty

In this analysis, systematic uncertainties on the measured v_2 are considered for the CNT arm selection, pad-chamber matching width, FVTX track DCA$_R$, and pileup rejection using the timing information of hit tubes in the BBCS. The central v_2 values are calculated using both the east and west CNT arms, pad-chamber matching width of 2σ, $|\mathrm{DCA}_R| < 2$ cm, and BBC timing fraction $f > 0.9$. The systematic uncertainty associated with CNT arm selection is obtained from the difference between v_2 in the east and west CNT arms. The systematic uncertainty associated with the pad-chamber matching is estimated by varying the matching width from 1.5σ to 2.5σ. The systematic uncertainty associated with the FVTX DCA$_R$ cut is estimated by varying the DCA$_R$ cut from 1.5 cm to 2.5 cm. Finally, the systematic uncertainty associated with pileup rejection is estimated by varying the BBC-timing-fraction cut from $f > 0.85$ to $f > 0.95$. Given the limited statistical precision at high-p_T, the systematic uncertainty is determined for $p_T < 3$ GeV/c and is applied to the entire p_T region.

The CNT arm selection is the largest source of systematic uncertainty and has an effect of up to 12% depending on collision system and centrality. The pad-chamber matching window and BBC-timing-fraction cuts have effects on the order of a few percent. The FVTX DCA$_R$ cuts have an effect of less than one percent in most cases. Each systematic

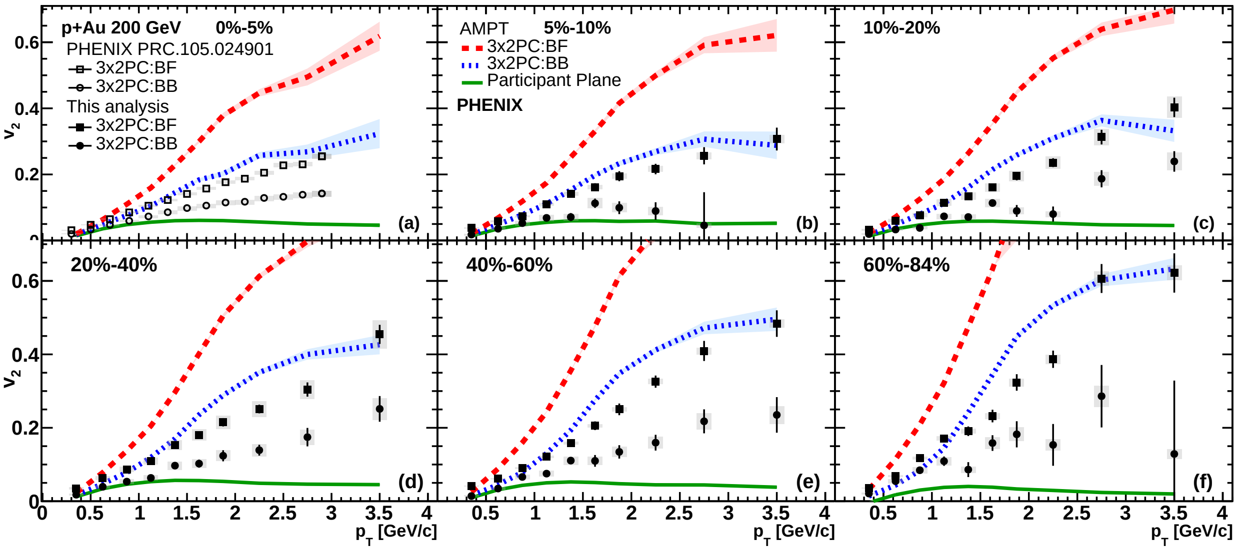

FIG. 4. Second-harmonic azimuthal anisotropy $v_2\{3\times 2\text{PC}\}$ in (a) 0%–5% [24], (b) 5%–10%, (c) 10%–20%, (d) 20%–40%, (e) 40%–60%, and (f) 60%–88% centrality p+Au collisions at $\sqrt{s_{NN}} = 200$ GeV with the FVTXS-CNT-FVTXN (BF) and BBCS-FVTXS-CNT (BB) detector combinations as a function of p_T. The solid [black] squares are shifted for visibility. The bands around the [black] squares and [black] circles show the systematic uncertainties. The bands around the dashed [red] and dotted [blue] curves show statistical uncertainties in the AMPT calculations with the 3×2PC method. The solid [green] curves show v_2 in AMPT using the parton participant plane.

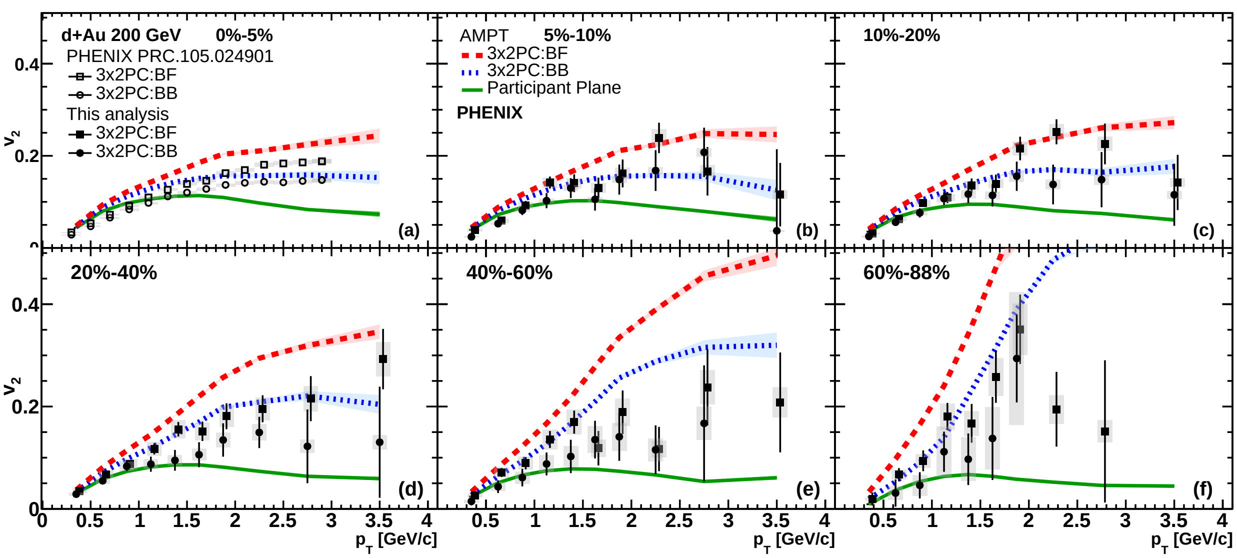

FIG. 5. Second-harmonic azimuthal anisotropy $v_2\{3\times 2\text{PC}\}$ in (a) 0%–5% [24], (b) 5%–10%, (c) 10%–20%, (d) 20%–40%, (e) 40%–60%, and (f) 60%–88% centrality d+Au collisions at $\sqrt{s_{NN}} = 200$ GeV with the FVTXS-CNT-FVTXN (BF) and BBCS-FVTXS-CNT (BB) detector combinations as a function of p_T. The solid [black] squares are shifted for visibility. The bands around the [black] squares and [black] circles show the systematic uncertainties. The bands around the dashed [red] and dotted [blue] curves show statistical uncertainties in the AMPT calculations with the 3×2PC method. The solid [green] curves show v_2 in AMPT using the parton participant plane.

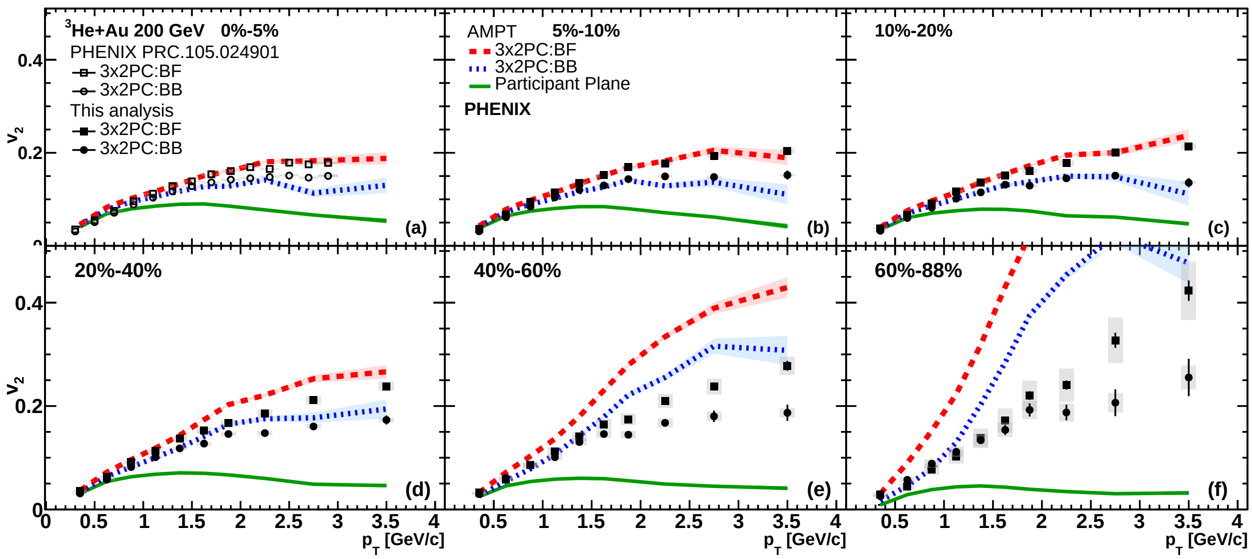

FIG. 6. Second-harmonic azimuthal anisotropy $v_2\{3 \times 2\mathrm{PC}\}$ in (a) 0%–5% [24], (b) 5%–10%, (c) 10%–20%, (d) 20%–40%, (e) 40%–60%, and (f) 60%–88% centrality ^{3}He+Au collisions at $\sqrt{s_{NN}} = 200$ GeV with the FVTXS-CNT-FVTXN (BF) and BBCS-FVTXS-CNT (BB) detector combinations as a function of p_T. The solid [black] squares are shifted for visibility. The bands around the [black] squares and [black] circles show the systematic uncertainties. The bands around the dashed [red] and dotted [blue] curves show statistical uncertainties in the AMPT calculations with the 3×2PC method. The solid [green] curves show v_2 in AMPT using the parton participant plane.

uncertainty is added in quadrature to obtain the total systematic uncertainty.

III. RESULTS

The experimental v_2 for midrapidity charged particles in p+p, p+Au, d+Au, and ^{3}He+Au collisions at $\sqrt{s_{NN}} = 200$ GeV is presented as a function of p_T, centrality, and event multiplicity. Then, the experimental results are compared to AMPT-model simulations and physics implications are discussed. Noting that previous flow extractions were restricted to 0%–5% central p+Au, d+Au, and ^{3}He+Au collisions, estimates of nonflow contributions indicated flow dominance. In the present analysis, pushing to lower multiplicities, including p+p collisions, it is expected that nonflow will have a larger role and become dominant, for example in p+p collisions. Thus, extraction of the second Fourier coefficient as v_2 should not necessarily be interpreted as flow, but rather an interplay of different effects.

A. p_T Dependence

Shown in Figs. 4, 5, and 6 is v_2 with the 3×2PC method as a function of p_T in different centrality selections for p+Au, d+Au, and ^{3}He+Au collisions at $\sqrt{s_{NN}} = 200$ GeV, respectively. The results in the 0%–5% most-central collisions are from Ref. [24]. Notably, nonzero v_2 is observed over the entire measured p_T range from most-central to most-peripheral collisions in these systems, with both the BB and BF detector combinations.

The kinematic dependence seen in 0%–5% central collisions, i.e. larger $v_2\{3 \times 2\mathrm{PC}\}$ with the BF combination ($v_2\{\mathrm{BF}\}$) than that with the BB combination ($v_2\{\mathrm{BB}\}$), is also observed in noncentral p+Au and ^{3}He+Au collisions. This trend becomes visible above $p_T = 0.5$ GeV/c in p+Au collisions and above $p_T = 1.5$ GeV/c in ^{3}He+Au collisions. These observations in noncentral p+Au and ^{3}He+Au collisions confirm the interpretation of the kinematic dependence discussed in Ref. [24]: the smaller multiplicity in the FVTXN acceptance relative to that in the BBCS acceptance results in more nonflow which makes the observed v_2 larger. The larger rapidity gap between FVTXS and FVTXN compared to that between BBCS and FVTXS also increases the event-plane decorrelation effects, which makes the denominator of Eq. (8) smaller. However, the factorization of the decorrelation effects between the numerator and denominator is under discussion [25] and thus the influence on v_2 is inconclusive. In contrast, the relation of $v_2\{\mathrm{BF}\} = v_2\{\mathrm{BB}\}$ holds below $p_T < 1.5$ GeV/c in ^{3}He+Au collisions. Note that no kinematic dependence is observed in noncentral d+Au collisions due to the limited statistical precision.

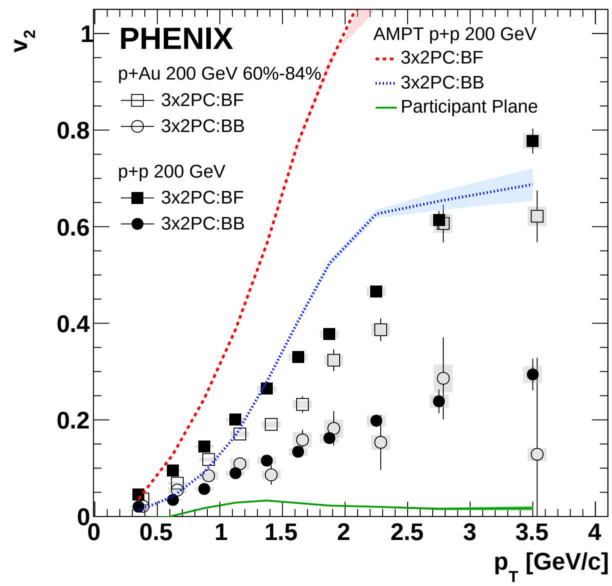

FIG. 7. Second-harmonic azimuthal anisotropy v_2 with the 3×2PC method in (open symbols) 60%–84% central p+Au collisions and (solid symbols) MB p+p collisions at $\sqrt{s_{NN}} = 200$ GeV with the FVTXS-CNT-FVTXN (BF) and BBCS-FVTXS-CNT (BB) detector combinations as a function of p_T. The open [black] squares and [black] circles are shifted for visibility. The solid bands around the [black] circles and [black] squares show experimental systematic uncertainties. The bands around the dashed [red] and dotted [blue] curves show statistical uncertainties in the AMPT calculations with the 3×2PC method in p+p collisions. The solid [green] curve shows v_2 in AMPT using the parton participant plane in p+p collisions.

Measurement of v_2 with the 3×2PC method is further extended to MB p+p collisions as shown in Fig. 7. Similar to the other collision systems, nonzero v_2 is observed over the entire measured p_T range for both the BB and BF detector combinations. At $p_T = 3.5$ GeV/c, the value of $v_2\{\mathrm{BB}\}$ remains at 0.3 while that of $v_2\{\mathrm{BF}\}$ soars to 0.8. The latter value larger than 0.5 indicates that correlations from back-to-back jets are dominant in this kinematic range. The magnitude of v_2 in p+p collisions is found to be similar to that of v_2 in 60%–84% central p+Au collisions.

B. Multiplicity Dependence

Figure 8 shows v_2 with the 3×2PC method in $0.5 < p_T < 1$ GeV/c and $2 < p_T < 2.5$ GeV/c as a function of centrality in p+Au, d+Au, and ^{3}He+Au collisions. In d+Au and ^{3}He+Au collisions, v_2 in $0.5 < p_T < 1$ GeV/c is generally flat over the entire measured centrality range within uncertainties. Only v_2 in p+Au collisions shows an increasing trend towards peripheral collisions for both the BB and BF detector combinations. In $2 < p_T < 2.5$ GeV/c, v_2 in p+Au and ^{3}He+Au collisions show increasing trends towards peripheral collisions for both the BB and BF detector combinations. In d+Au collisions, this trend is not observed because of the limited statistical precision.

Figure 9 shows that a point-by-point comparison among the different collision systems can be made with the 3×2PC method using both the BB and BF detector combinations by plotting v_2 as a function of charged particle multiplicity $\frac{dN_{ch}}{d\eta}$ at midrapidity. The values of $\frac{dN_{ch}}{d\eta}$ are obtained from Ref. [31]. In $2 < p_T < 2.5$ GeV/c, $v_2\{\mathrm{BB}\}$ shows an increasing trend towards the low $\frac{dN_{ch}}{d\eta}$ side; the peripheral p+Au data points smoothly connect to the p+p data point within uncertainties. This trend is more clearly seen in $v_2\{\mathrm{BF}\}$ for both $0.5 < p_T < 1$ GeV/c and $2 < p_T < 2.5$ GeV/c. Above $\frac{dN_{ch}}{d\eta} = 10$, these series of v_2 measurements generally show flat trends. Unlike these trends, $v_2\{\mathrm{BB}\}$ in $0.5 < p_T < 1$ GeV/c shows a flat shape over the entire measured $\frac{dN_{ch}}{d\eta}$ range within the current experimental uncertainties, which might indicate that the balance of nonflow effects between the numerator and denominator of Eq. (8) stays the same in this $\frac{dN_{ch}}{d\eta}$ range.

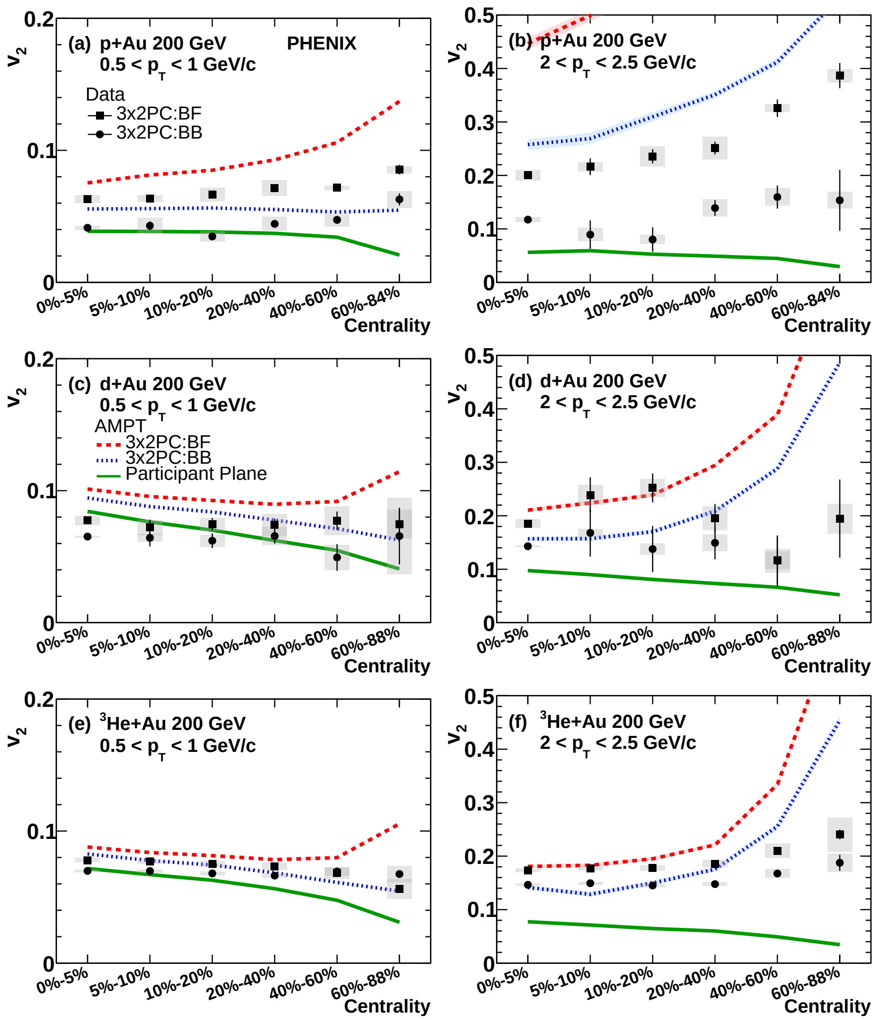

FIG. 8. Second-harmonic azimuthal anisotropy $v_2\{3 \times 2\text{PC}\}$ as a function of centrality in (a,b) p+Au, (c,d) d+Au, and (e,f) ^{3}He+Au collisions at $\sqrt{s_{NN}} = 200$ GeV with the FVTXS-CNT-FVTXN (BF) and BBCS-FVTXS-CNT (BB) detector combinations. The bands around the [black] circles and [black] squares show experimental systematic uncertainties. The bands around the dashed [red] and dotted [blue] curves show statistical uncertainties in the AMPT calculations with the 3×2PC method. The solid [green] curves show v_2 in AMPT using the parton participant plane.

Finally, the kinematic dependence of v_2 is quantified by the ratio R of v_2 in the BF detector combination to that in the BB combination. Figure 10 shows R as a function of charged-particle multiplicity $\frac{dN_{ch}}{d\eta}$ at midrapidity for $0.5 < p_T < 1$ GeV/c and $2 < p_T < 2.5$ GeV/c. In $0.5 < p_T < 1$ GeV/c, R in d+Au and ^{3}He+Au collisions approaches unity as $\frac{dN_{ch}}{d\eta}$ increases, indicating weak kinematic dependence, i.e. the restoration of flow factorization. Towards the low $\frac{dN_{ch}}{d\eta}$ side, R in ^{3}He+Au collisions falls below unity, however R in p+Au and d+Au collisions do not show clear trends due to the limited statistical and systematic precision. At the lowest $\frac{dN_{ch}}{d\eta}$, R in p+p collisions shows the largest value among these collision systems. In $2 < p_T < 2.5$ GeV/c, the R values in d+Au and ^{3}He+Au collisions are consistent within uncertainties in the overlapping $\frac{dN_{ch}}{d\eta}$ region. The measured R is generally larger in p+Au than in d+Au and ^{3}He+Au collisions even in the overlapping $\frac{dN_{ch}}{d\eta}$ ranges. For the lowest values of $\frac{dN_{ch}}{d\eta}$, the values of R in p+p and p+Au collisions are consistent within uncertainties. The different trends of R between $0.5 < p_T < 1$ GeV/c and $2 < p_T < 2.5$ GeV/c likely indicate that the kinematic dependence is caused by different underlying mechanisms.

C. Comparison With AMPT Model Simulations

To further investigate the experimental v_2 results, the AMPT model is employed with string melting turned on and the parton-parton interaction cross section set to 1.5 mb. We used the same AMPT parameter settings as those used in Ref. [13] for its v_2 study in the d+Au beam energy scan. In this AMPT model calculation, final-state particle v_2 is calculated using the 3×2PC method with the same p_T and rapidity range selections as the experimental measurements, as well as relative to the parton participant plane determined using initial partons. We use the parton participant plane v_2 as a proxy of pure collective development of the collision system, which is likely to underestimate the true v_2

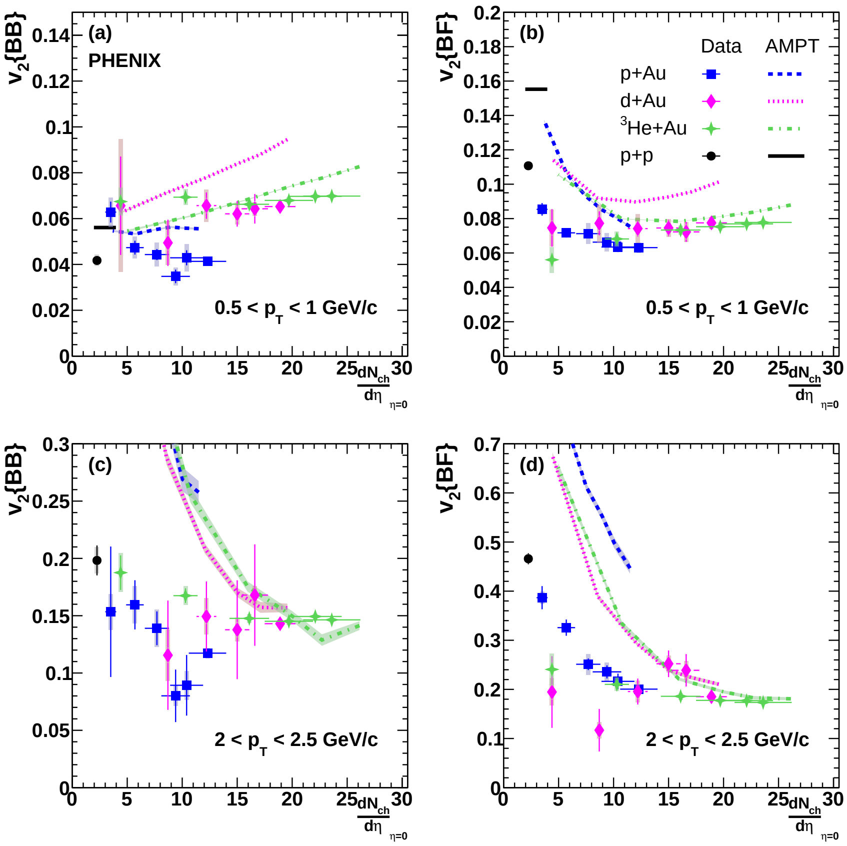

FIG. 9. Second-harmonic azimuthal anisotropy $v_2\{3\times 2\mathrm{PC}\}$ as a function of charged-particle multiplicity $\frac{dN_{ch}}{d\eta}$ at midrapidity in p+p, p+Au, d+Au, and ^{3}He+Au collisions at $\sqrt{s_{NN}}$ = 200 GeV with (a,c) the BBCS-FVTXS-CNT (BB) and (b,d) FVTXS-CNT-FVTXN (BF) detector combinations. The bands around the data points show experimental systematic uncertainties and the bands around the curves show statistical uncertainties in the AMPT calculations. Note that AMPT results for p+p collisions in (c) and (d) are outside of the plot range due to their large values.

value. The difference between v_2 relative to the parton participant plane and that with the 3×2PC method in AMPT model can provide some insight on the relative contributions from nonflow and event-plane decorrelation effects. Note that the experimental event trigger efficiency has not been applied to peripheral small systems and p+p collisions in this AMPT simulation and thus the full inelastic cross section was used in this study.

1. p_T Dependence

Figures 4, 5, and 6 show comparisons of AMPT v_2 with the experimental measurements as a function of p_T. The v_2 calculated from AMPT with the 3×2PC method generally describes the experimental v_2 results from most-central to midcentral d+Au and ^{3}He+Au collisions. However, it overshoots the data in all centralities for p+Au collisions and in midcentral to peripheral centralities for d+Au and ^{3}He+Au collisions, similar to what was previously reported in Ref [13] for peripheral d+Au collisions, indicating much higher levels of nonflow in AMPT compared to the data. An explanation for this overestimate is that the HIJING model, used to describe hard-scattering processes in AMPT, is known to have a wider near-side jet correlation than in real p+p data [32]. This mismatch of the jet kinematics leads to this overestimate. While v_2 relative to the parton participant plane weakly depends on p_T, its difference from v_2 with the 3×2PC method increases with increasing p_T, indicating stronger nonflow at high p_T.

The AMPT-model calculations are in quantitative agreement with the kinematic dependence of v_2 in these collision systems, indicating the breaking of flow factorization in this model. In midcentral to peripheral ^{3}He+Au collisions, below $p_T < 1.5$ GeV/c, the AMPT model shows a clear separation between v_2\{BF\} and v_2\{BB\} unlike the experimental data, again indicating an overestimate of nonflow and decorrelation effects in this model.

As shown in Fig. 7, the AMPT model v_2 with the 3×2PC method also overestimates the experimental data in p+p collisions, similar to the comparison made for the peripheral p+Au collision case. Again this overestimate may be attributable to the jet kinematics mismatch in the HIJING model used in AMPT [32]. The large gap between v_2 relative to the parton participant plane and that with the 3×2PC method indicates nonflow is dominant in p+p collisions in the AMPT model.

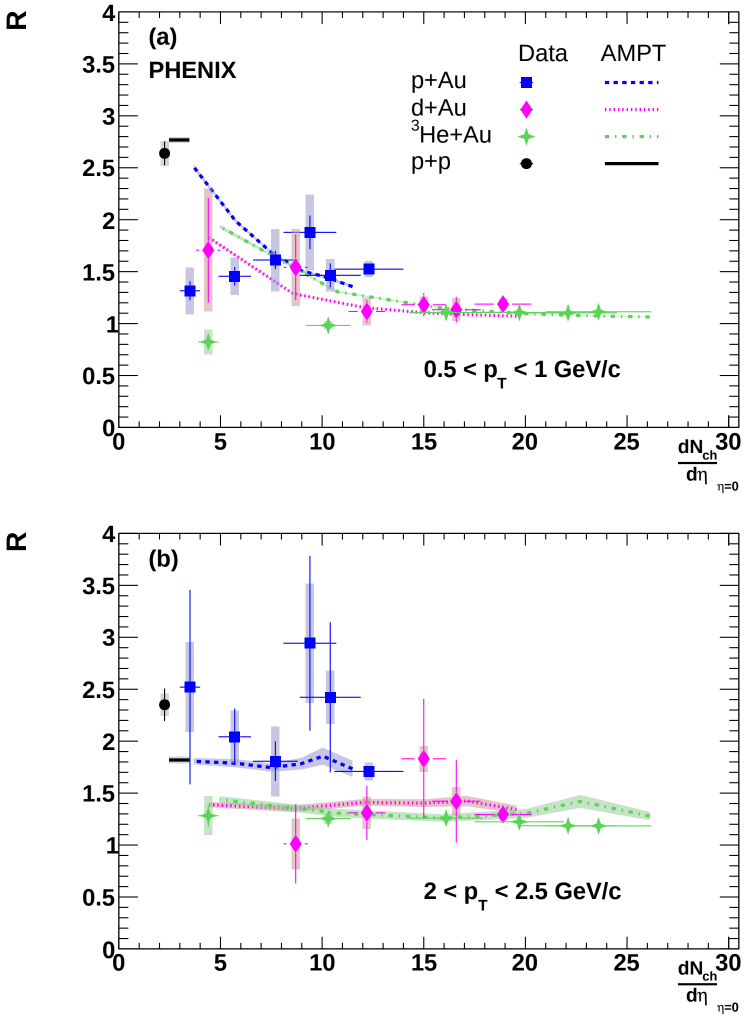

FIG. 10. The ratio R of $v_2\{\mathrm{BF}\}$ to $v_2\{\mathrm{BB}\}$ as a function of charged-particle multiplicity $\frac{dN_{ch}}{d\eta}$ at midrapidity in (squares) p+Au, (diamonds) d+Au, (crosses) ^{3}He+Au and (circles) p+p collisions at $\sqrt{s_{NN}} = 200$ GeV. The bands around the data points show experimental systematic uncertainties and the bands around the curves show statistical uncertainties in the AMPT calculations.

2. Multiplicity Dependence

Figure 8 shows a comparison of AMPT v_2 with the experimental results as a function of centrality. In $0.5 < p_T < 1$ GeV/c, the AMPT model v_2 with the BB detector combination shows a flat trend in p+Au collisions and slight decreasing trends in d+Au and ^{3}He+Au collisions over the entire measured centrality ranges, which is inconsistent with the experimental data. In contrast, v_2 with the BF detector combination shows an increasing trend towards the most peripheral collisions. For $2 < p_T < 2.5$ GeV/c, the AMPT model v_2 with both detector combinations qualitatively captures the increasing trends in the experimental data.

Figure 9 shows a comparison of AMPT v_2 with the experimental results as a function of $\frac{dN_{ch}}{d\eta}$. As seen in the centrality dependence of v_2, the AMPT model generally fails to reproduce the qualitative trends of $v_2\{\mathrm{BB}\}$ in $0.5 < p_T < 1$ GeV/c while it captures the increasing trends of $v_2\{\mathrm{BB}\}$ in $2 < p_T < 2.5$ GeV/c and $v_2\{\mathrm{BF}\}$ in both $0.5 < p_T < 1$ GeV/c and $2 < p_T < 2.5$ GeV/c towards smaller systems (and hence lower multiplicities). The AMPT simulations also show an increase of $v_2\{\mathrm{BB}\}$ and $v_2\{\mathrm{BF}\}$ for $0.5 < p_T < 1$ GeV/c with increasing multiplicity above $\frac{dN_{ch}}{d\eta} = 10$. This reflects the dominance of collective expansion at low-p_T in the AMPT model.

Finally, Fig. 10 shows a comparison of the R value calculated in AMPT with the experimental results as a function of $\frac{dN_{ch}}{d\eta}$. For $0.5 < p_T < 1$ GeV/c, the AMPT model simulations show an increasing trend in R as $\frac{dN_{ch}}{d\eta}$ decreases, which is contradicted by the experimental data. However, the AMPT model is in agreement with the flow factorization seen in the experimental data at high $\frac{dN_{ch}}{d\eta}$. For $2 < p_T < 2.5$ GeV/c, the AMPT model calculations qualitatively capture the trends of the measured R values.

IV. SUMMARY

In summary, measurements of azimuthal anisotropy v_2 were presented as a function of p_T, centrality, and charged-particle multiplicity in MB p+p and noncentral p+Au, d+Au, and ^{3}He+Au collisions at $\sqrt{s_{_{NN}}} = 200$ GeV using the 3×2PC method. The previous experimental findings that $v_2\{\text{BF}\} > v_2\{\text{BB}\}$ is also found in peripheral collisions in p+Au, d+Au, and ^{3}He+Au as well as in MB p+p collisions. This indicates smaller nonflow contribution in the BB combination and much more substantial nonflow contribution in the BF combination, in concurrence with the conclusions of Refs. [24, 25]. The possible contributions to these v_2 from the nonflow between the backward detectors and longitudinal decorrelation effects between the backward and forward detectors are under discussion [24, 25] towards precise quantification of these effects. The kinematic dependence of v_2 is quantified as the ratio R of v_2 between the two detector combinations as a function of $\frac{dN_{ch}}{d\eta}$ for $0.5 < p_T < 1$ and $2 < p_T < 2.5$ GeV/c. The different trend of R between these p_T selections suggests strong p_T dependence of nonflow effects. The AMPT model calculations can quantitatively describe the experimental measurements only in most-central to midcentral d+Au and ^{3}He+Au collisions, and it systematically overestimates in p+Au and p+p collisions, indicating an unrealistically high nonflow contribution in AMPT. These measurements in various collision systems with different fractions of prehydrodynamization, nonflow, and decorrelation effects may serve as references for future unified models incorporating initial-state effects, prehydrodynamization dynamics, hydrodynamic expansion, and jets.

ACKNOWLEDGMENTS

We thank the staff of the Collider-Accelerator and Physics Departments at Brookhaven National Laboratory and the staff of the other PHENIX participating institutions for their vital contributions. We acknowledge support from the Office of Nuclear Physics in the Office of Science of the Department of Energy, the National Science Foundation, Abilene Christian University Research Council, Research Foundation of SUNY, and Dean of the College of Arts and Sciences, Vanderbilt University (USA), Ministry of Education, Culture, Sports, Science, and Technology and the Japan Society for the Promotion of Science (Japan), Natural Science Foundation of China (People's Republic of China), Croatian Science Foundation and Ministry of Science and Education (Croatia), Ministry of Education, Youth and Sports (Czech Republic), Centre National de la Recherche Scientifique, Commissariat à l'Énergie Atomique, and Institut National de Physique Nucléaire et de Physique des Particules (France), J. Bolyai Research Scholarship, EFOP, the New National Excellence Program (ÚNKP), NKFIH, and OTKA (Hungary), Department of Atomic Energy and Department of Science and Technology (India), Israel Science Foundation (Israel), Basic Science Research and SRC(CENuM) Programs through NRF funded by the Ministry of Education and the Ministry of Science and ICT (Korea), Ministry of Education and Science, Russian Academy of Sciences, Federal Agency of Atomic Energy (Russia), VR and Wallenberg Foundation (Sweden), University of Zambia, the Government of the Republic of Zambia (Zambia), the U.S. Civilian Research and Development Foundation for the Independent States of the Former Soviet Union, the Hungarian American Enterprise Scholarship Fund, the US-Hungarian Fulbright Foundation, and the US-Israel Binational Science Foundation.

---

[1] K. Adcox *et al.* (PHENIX Collaboration), Formation of dense partonic matter in relativistic nucleus-nucleus collisions at RHIC: Experimental evaluation by the PHENIX collaboration, Nucl. Phys. A **757**, 184 (2005).

[2] I. Arsene *et al.* (BRAHMS Collaboration), Quark gluon plasma and color glass condensate at RHIC? The Perspective from the BRAHMS experiment, Nucl. Phys. A **757**, 1 (2005).

[3] B. B. Back, M. D. Baker, M. Ballintijn, D. S. Barton, B. Becker, *et al.*, The PHOBOS perspective on discoveries at RHIC, Nucl. Phys. A **757**, 28 (2005).

[4] J. Adams *et al.* (STAR Collaboration), Experimental and theoretical challenges in the search for the quark gluon plasma: The STAR Collaboration's critical assessment of the evidence from RHIC collisions, Nucl. Phys. A **757**, 102 (2005).

[5] P. Romatschke, New Developments in Relativistic Viscous Hydrodynamics, Int. J. Mod. Phys. E **19**, 1 (2010).

[6] U. Heinz and R. Snellings, Collective flow and viscosity in relativistic heavy-ion collisions, Ann. Rev. Nucl. Part. Sci. **63**, 123 (2013).

[7] G. Aad *et al.* (ATLAS Collaboration), Observation of Associated Near-Side and Away-Side Long-Range Correlations in $\sqrt{s_{NN}}$=5.02 TeV Proton-Lead Collisions with the ATLAS Detector, Phys. Rev. Lett. **110**, 182302 (2013).

[8] B. Abelev *et al.* (ALICE Collaboration), Long-range angular correlations on the near and away side in $p-$Pb collisions at $\sqrt{s_{NN}} = 5.02$ TeV, Phys. Lett. B **719**, 29 (2013).

[9] S. Chatrchyan *et al.* (CMS Collaboration), Observation of Long-Range Near-Side Angular Correlations in Proton-Lead Collisions at the LHC, Phys. Lett. B **718**, 795 (2013).

[10] A. Adare *et al.* (PHENIX Collaboration), Quadrupole Anisotropy in Dihadron Azimuthal Correlations in Central d+Au Collisions at $\sqrt{s_{NN}}$=200 GeV, Phys. Rev. Lett. **111**, 212301 (2013).

[11] J. L. Nagle, A. Adare, S. Beckman, T. Koblesky, J. Orjuela Koop, D. McGlinchey, P. Romatschke, J. Carlson, J. E. Lynn, and M. McCumber, Exploiting Intrinsic Triangular Geometry in Relativistic ^{3}He+Au Collisions to Disentangle Medium Properties, Phys. Rev. Lett. **113**, 112301 (2014).

[12] C. Aidala *et al.* (PHENIX Collaboration), Measurement of long-range angular correlations and azimuthal anisotropies in high-multiplicity p+Au collisions at $\sqrt{s_{NN}} = 200$ GeV, Phys. Rev. C **95**, 034910 (2017).

[13] C. Aidala *et al.* (PHENIX Collaboration), Measurements of azimuthal anisotropy and charged-particle multiplicity in d+Au collisions at $\sqrt{s_{NN}}$ =200, 62.4, 39, and 19.6 GeV, Phys. Rev. C **96**, 064905 (2017).

[14] A. Adare *et al.* (PHENIX Collaboration), Measurements of elliptic and triangular flow in high-multiplicity ^{3}He+Au collisions at $\sqrt{s_{NN}} = 200$ GeV, Phys. Rev. Lett. **115**, 142301 (2015).

[15] A. Adare *et al.* (PHENIX Collaboration), Measurement of long-range angular correlation and quadrupole anisotropy of pions and (anti)protons in central d+Au collisions at $\sqrt{s_{NN}}$=200 GeV, Phys. Rev. Lett. **114**, 192301 (2015).

[16] C. Aidala *et al.* (PHENIX Collaboration), Creation of quark–gluon plasma droplets with three distinct geometries, Nature Phys. **15**, 214 (2019).

[17] J. Adam *et al.* (STAR Collaboration), Azimuthal Harmonics in Small and Large Collision Systems at RHIC Top Energies, Phys. Rev. Lett. **122**, 172301 (2019).

[18] C. Shen, J.-F. Paquet, G. S. Denicol, S. Jeon, and C. Gale, Collectivity and electromagnetic radiation in small systems, Phys. Rev. C **95**, 014906 (2017).

[19] M. Mace, V. V. Skokov, P. Tribedy, and R. Venugopalan, Hierarchy of Azimuthal Anisotropy Harmonics in Collisions of Small Systems from the Color Glass Condensate, Phys. Rev. Lett. **121**, 052301 (2018), [Phys. Rev. Lett. **123**, 039901(E) (2019)].

[20] M. Mace, V. V. Skokov, P. Tribedy, and R. Venugopalan, Systematics of azimuthal anisotropy harmonics in proton–nucleus collisions at the LHC from the Color Glass Condensate, Phys. Lett. B **788**, 161 (2019), [Phys. Lett. B **799**, 135006(E) (2019)].

[21] B. Schenke, C. Shen, and P. Tribedy, Hybrid Color Glass Condensate and hydrodynamic description of the Relativistic Heavy Ion Collider small system scan, Phys. Lett. B **803**, 135322 (2020).

[22] M. Habich, J. L. Nagle, and P. Romatschke, Particle spectra and HBT radii for simulated central nuclear collisions of C+C, Al+Al, Cu+Cu, Au+Au, and Pb+Pb from $\sqrt{s} = 62.4$–2760 GeV, Eur. Phys. J. C **75**, 15 (2015).

[23] P. Romatschke, Light-Heavy Ion Collisions: A window into pre-equilibrium QCD dynamics?, Eur. Phys. J. C **75**, 305 (2015).

[24] U. Acharya *et al.* (PHENIX Collaboration), Kinematic dependence of azimuthal anisotropies in p+Au, d+Au, ^{3}He+Au at $\sqrt{s_{NN}} = 200$ GeV, Phys. Rev. C **105**, 024901 (2022).

[25] J. L. Nagle, R. Belmont, S. H. Lim, and B. Seidlitz, Checking nonflow assumptions and results via PHENIX published correlations in $p + p, p$+Au, d+Au, and ^{3}He+Au at $\sqrt{s_{NN}}$=200 GeV, Phys. Rev. C **105**, 024906 (2022).

[26] Z.-W. Lin, C. M. Ko, B.-A. Li, B. Zhang, and S. Pal, A Multi-phase transport model for relativistic heavy ion collisions, Phys. Rev. C **72**, 064901 (2005).

[27] K. Adcox *et al.* (PHENIX Collaboration), PHENIX detector overview, Nucl. Instrum. Methods Phys. Res., Sec. A **499**, 469 (2003).

[28] C. Aidala *et al.*, The PHENIX Forward Silicon Vertex Detector, Nucl. Instrum. Methods Phys. Res., Sec. A **755**, 44 (2014).

[29] M. Allen *et al.* (PHENIX Collaboration), PHENIX inner detectors, Nucl. Instrum. Methods Phys. Res., Sec. A **499**, 549 (2003).

[30] A. Adare *et al.* (PHENIX Collaboration), Centrality categorization for $R_{p(d)+A}$ in high-energy collisions, Phys. Rev. C **90**, 034902 (2014).

[31] A. Adare *et al.* (PHENIX Collaboration), Pseudorapidity Dependence of Particle Production and Elliptic Flow in Asymmetric Nuclear Collisions of p+Al, p+Au, d+Au, and ^{3}He+Au at $\sqrt{s_{NN}} = 200$ GeV, Phys. Rev. Lett. **121**, 222301 (2018).

[32] S. H. Lim, Q. Hu, R. Belmont, K. K. Hill, J. L. Nagle, and D. V. Perepelitsa, Examination of flow and nonflow factorization methods in small collision systems, Phys. Rev. C **100**, 024908 (2019).